Reorganization of lamina-associated domains in early mouse embryos is regulated by RNA polymerase II activity

Mrinmoy Pal,[1] Luis Altamirano-Pacheco,[1] Tamas Schauer,[1] and Maria-Elena Torres-Padilla[1,2]

[1]Institute of Epigenetics and Stem Cells (IES), Helmholtz Zentrum München, D-81377 München, Germany; [2]Faculty of Biology, Ludwig-Maximilians Universität, D-81377 München, Germany

Fertilization in mammals is accompanied by an intense period of chromatin remodeling and major changes in nuclear organization. How the earliest events in embryogenesis, including zygotic genome activation (ZGA) during maternal-to-zygotic transition, influence such remodeling remains unknown. Here, we have investigated the establishment of nuclear architecture, focusing on the remodeling of lamina-associated domains (LADs) during this transition. We report that LADs reorganize gradually in two-cell embryos and that blocking ZGA leads to major changes in nuclear organization, including altered chromatin and genomic features of LADs and redistribution of H3K4me3 toward the nuclear lamina. Our data indicate that the rearrangement of LADs is an integral component of the maternal-to-zygotic transition and that transcription contributes to shaping nuclear organization at the beginning of mammalian development.

[*Keywords*: ZGA; nuclear organization; lamina-associated domain; embryonic development]

Supplemental material is available for this article.

Received May 15, 2023; revised version accepted October 12, 2023.

In mammals, development begins upon fertilization of the oocyte by the sperm, two highly differentiated cells, and gives rise to the one-cell embryo, or zygote. After fertilization, the chromatin of the two gametes undergoes an intense period of chromatin remodeling, which is essential to start a new developmental program. As part of this remodeling, histone modifications are reset and re-established genome-wide with different developmental kinetics, a process that continues until at least 3.5 d later at the blastocyst stage (Burton and Torres-Padilla 2014; Xia and Xie 2020). For example, the oocyte is characterized by broad H3K4me3 domains, which are inherited by the zygote and are largely remodeled during the first two embryonic cell divisions (Dahl et al. 2016; Liu et al. 2016; Zhang et al. 2016). In addition, heterochromatin progressively matures and the patterns of H3K27me3 and H3K9me3 emerge gradually during preimplantation development (Liu et al. 2016; Wang et al. 2018; Burton et al. 2020). This time window is also characterized by a robust expression of transposable elements (Peaston et al. 2004; Fadloun et al. 2013) with H3K4me3 peaks known to be enriched for repeats in mouse preimplantation embryos (Zhang et al. 2016).

Early development is initially supported by maternal transcripts, which are synthesized during oocyte growth and inherited by the embryo. The embryo transitions away from the dependence on maternal supplies in a process referred to as maternal-to-zygotic transition (MZT) (Schultz 2002; Li et al. 2013; Vastenhouw et al. 2019). MZT occurs through several processes, including the activation of the embryonic genome and the degradation of maternal transcripts. In mice, embryonic genome activation, referred to as zygotic genome activation (ZGA), occurs in two waves: A minor wave of transcriptional activation occurs at the late zygote stage, and a major, more substantial transcriptional wave occurs at the late two-cell stage (Zeng and Schultz 2005; Abe et al. 2018; Schulz and Harrison 2019).

The 3D nuclear organization in the early embryo is also heavily remodeled (Pecori and Torres-Padilla 2023). In mice, A and B chromatin compartments are initially not well defined and compartment strength increases gradually during preimplantation development. Likewise, topologically associating domains (TADs) also mature progressively during this period, with TAD boundaries becoming progressively insulated as development proceeds (Du et al. 2017; Flyamer et al. 2017; Ke et al. 2017). Lamina-associated domains (LADs) are genomic regions that

Corresponding author: torres-padilla@helmholtz-muenchen.de
Article published online ahead of print. Article and publication date are online at http://www.genesdev.org/cgi/doi/10.1101/gad.350799.123.

make contact with the nuclear lamina (van Steensel and Belmont 2017) and can reshuffle stochastically after mitosis (Kind et al. 2013). Interestingly, LADs are rapidly established after fertilization, and thus LAD formation precedes consolidation of TADs. In fact, 67% of the LADs established in zygotes correspond to "constitutive" LADs (cLADs) (Borsos et al. 2019), which are cell-type-invariable LADs (Meuleman et al. 2013). However, LADs also become rearranged as development progresses, in particular at the late two-cell stage, where LADs have atypical features compared with cLADs and LADs in other cell types (Peric-Hupkes et al. 2010). For example, two-cell stage LADs are smaller and appear fragmented compared with the zygote stage and display distinctive genomic features, including relatively low CpG density and AT content (Borsos et al. 2019). Such unusual spatial arrangement is transient, as LADs in the four-cell stage do not show such features. Almost 42% of the zygotic LADs reposition to the nuclear interior at the two-cell stage, and two-cell-specific LADs emerge (Borsos et al. 2019). However, how such large-scale genome rearrangement is regulated, and whether developmental processes such as ZGA contribute to these changes in nuclear organization is not known.

Here, we analyzed the rearrangement of LADs that occurs during MZT and defined the role of zygotic genome activation in this process. Our work indicates that LAD reorganization in two-cell embryos is gradual and dynamic. By inhibiting ZGA with two different inhibitors, we show that transcriptional activity at ZGA contributes to LAD reorganization. Surprisingly, transcriptional inhibition of RNA polymerase II results in a redistribution of H3K4me3 domains to the nuclear periphery, which is accompanied by the large-scale repositioning of LAD boundaries and the sequestration of major ZGA genes at the nuclear lamina. Our work sheds light onto the molecular determinants of nuclear organization at the beginning of mammalian development.

Results

LAD reorganization in two-cell embryos is gradual and dynamic

To investigate the temporal definition and molecular regulators of the changes in nuclear organization that occur during ZGA, we focused on LADs. We previously mapped LADs in mouse zygotes before mitosis and in late two-cell stage embryos, which are separated by ~24 h. In order to obtain a better temporal resolution of LADs during development, we first mapped LADs in early two-cell stage embryos using LaminB1-DamID (Borsos et al. 2019), which corresponds to the end of G1 phase of the second embryonic cell cycle, prior to the major ZGA wave (Fig. 1A; Jukam et al. 2017; Schulz and Harrison 2019). Overall, genome-wide DamID values correlated equally to zygotes and to late two-cell stage embryos (Fig. 1B), suggesting that LADs have intermediate features between the two stages. In addition, despite their similar correlation, the range of DamID values in early two-cell stage is more similar to zygote than to late two-cell stage embryos (Fig. 1B). To investigate this further, we performed principal component analysis using the DamID methylation values (Fig. 1C), which indicated that early two-cell LaminB1-DamID values indeed separate between late two-cell stage and zygotes along PC2, while PC1 separates later developmental stages, including eight-cell stage and embryonic stem (ES) cells (Fig. 1C).

We next defined LADs based on the LaminB1-DamID values by using a hidden Markov model (HMM) as before (Meuleman et al. 2013). Visual inspection of LADs confirmed the expected fragmented LAD profile characteristic of late two-cell stage embryos, compared with zygotes (Fig. 1D; Borsos et al. 2019). Early two-cell LADs appeared to be of an intermediate nature, showing both small fragmented LADs and larger continuous LADs (Fig. 1D). Indeed, the median LAD length in early two-cell stage embryos was 1.8 Mb (interquartile range 0.9–3.6 Mb), compared with a median length of 2.25 and 0.9 Mb in zygotes and late two-cell stage embryos, respectively (Fig. 1E). In addition, the percentage of the genome located at the nuclear lamina in early two-cell stage embryos (42.12%) was intermediate between zygotes (36.40%) and late two-cell stage embryos (48.34%), potentially suggesting that the genome largely reorganizes by moving toward the nuclear lamina progressively during this stage (Fig. 1F). The average genomic AT content was clearly higher in early two-cell LADs compared with inter-LADs (iLADs) and was similar to the zygote (Fig. 1G). On the other hand, the pattern of gene density between LADs and iLADs in early two-cell embryos was more similar to the late two-cell stage embryo, in contrast to the zygote, in which iLADs displayed a much higher gene coverage compared with LADs (Fig. 1H). Finally, CpG density in early two-cell stage embryos displayed an intermediate enrichment in iLADs compared with zygotes and late two-cell stage embryos (Fig. 1I). Altogether, these data indicate that LADs at the two-cell stage mature gradually during the complete cell cycle with evolving molecular and genomic features. This suggests that dynamic rearrangement of genome–lamina contacts occurs during interphase progression. The latter is in line with recent work that has demonstrated that LADs evolve over the cell cycle in human cells in culture (van Schaik et al. 2020).

Repositioning of LADs following mitosis correlates with gene and TE class expression

To investigate the potential determinants and the dynamics of LAD reorganization upon the first mitosis and during the two-cell stage in more detail, we first examined whether and when LADs dislodge from the nuclear lamina (e.g., when they become iLADs) and vice versa. We found that rearrangement of the genomic regions in iLADs and LADs occurs both between zygotes and early two-cell stage embryos and between early and late two-cell stage embryos (Fig. 2A). For example, 19% of iLADs become LADs between zygotes and early two-cell stage and remain LADs at the late two-cell stage (iL-L-L) (Fig. 2A). However, we also found that 21% of zygotic iLADs

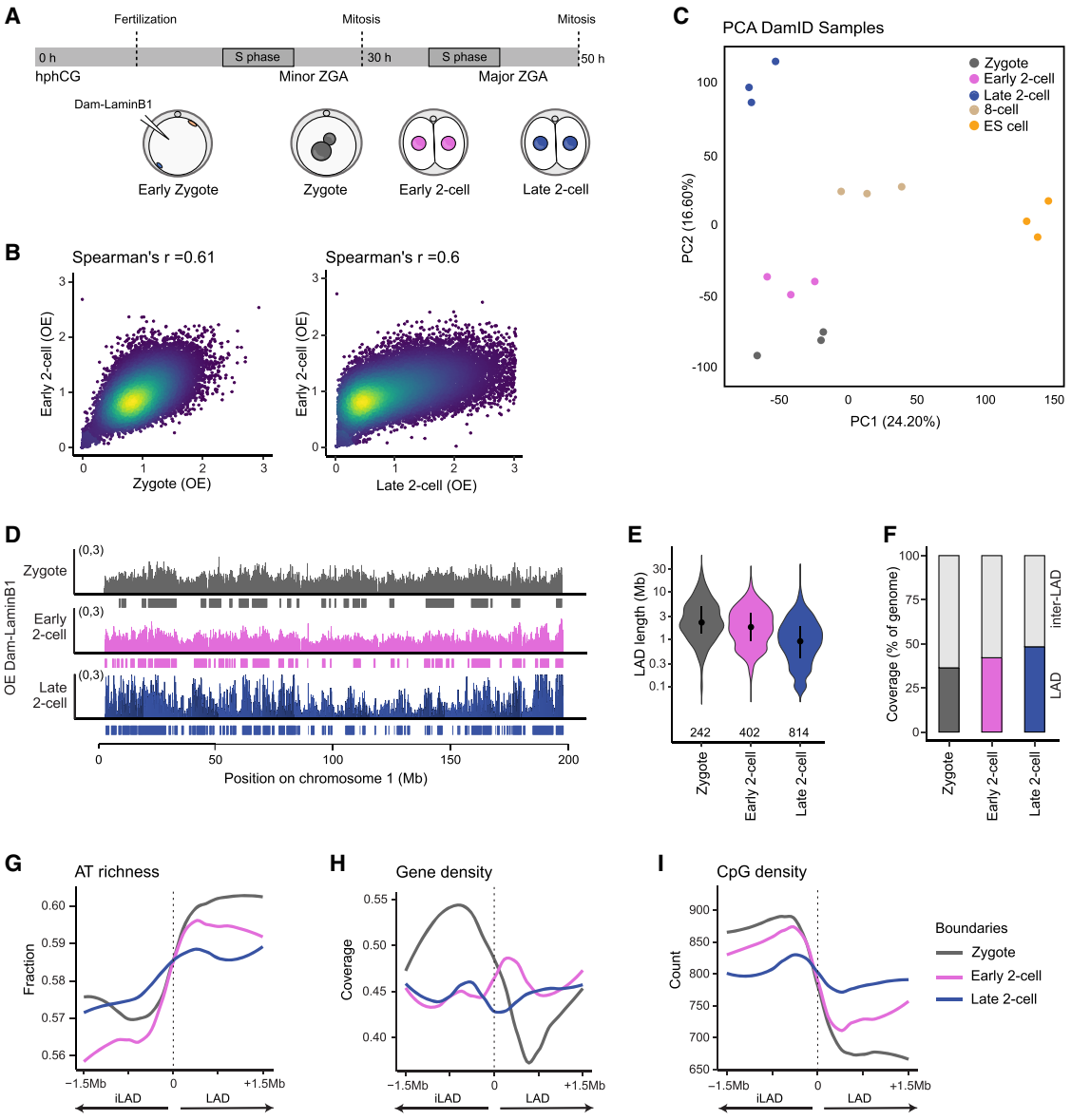

Figure 1. LAD reorganization in two-cell embryos is gradual and dynamic. (*A*) Schematic with time line of early development in mouse embryos and DamID collection time points. (hphCG) Hours post-hCG. (*B*) Genome-wide scatter plots (100-kb bins) of observed over expected (OE) Dam-LaminB1 mean scores from three biological replicates. Spearman's correlation coefficients are indicated. (*C*) Principal component analysis (PCA) of DamID samples. Zygote and late two-cell, eight-cell, and embryonic stem (ES) cell population DamID data analyzed from GSE112551 (Borsos et al. 2019). Each data point represents a biological replicate for the corresponding stages as indicated by the color code. The percentage of variance explained by PC1 and PC2 is indicated in the axis labels. (*D*) Dam-LaminB1 OE value profiles on chromosome 1. Boxes *below* the tracks represent LADs called by HMM. (*E*) Distribution of LAD length. Violin plots show the 25th and 75th percentiles (black lines) and median (circles). *n* indicates the number of LADs called, shown *below* the violin plots. (*F*) The percentage genomic coverage of LADs and iLADs. (*G–I*) Average AT content (*G*), gene coverage (*H*), and CpG density (*I*) (calculated in 100-kb genomic bins) over LAD boundaries of their own developmental stage. Zero and the dotted line represent the position of the LAD/iLAD boundary in the metaplot, and the 1.5-Mb region at the *right* indicates LAD.

remain iLADs in early two-cell stage embryos but become associated with the nuclear lamina at the late two-cell stage (iL-iL-L) (Fig. 2A). Additionally, only a small proportion of the genome (2.2%) behaves as "transient" early two-cell stage iLADs: These are regions that are LADs in zygotes and late two-cell stage embryos but dislodge from the nuclear lamina and are iLADs in early two-cell stage embryos (L-iL-L) (Fig. 2A). However, in line with our previous findings (Borsos et al. 2019), around half of the genome (57%) does not rearrange between zygotes and two-cell stage embryos—35% remain as LADs and 22% remain as iLADs (L-L-L and iL-iL-iL) (Fig. 2A). These data indicate that the rearrangements of the genome are progressive and occur both after the first embryonic

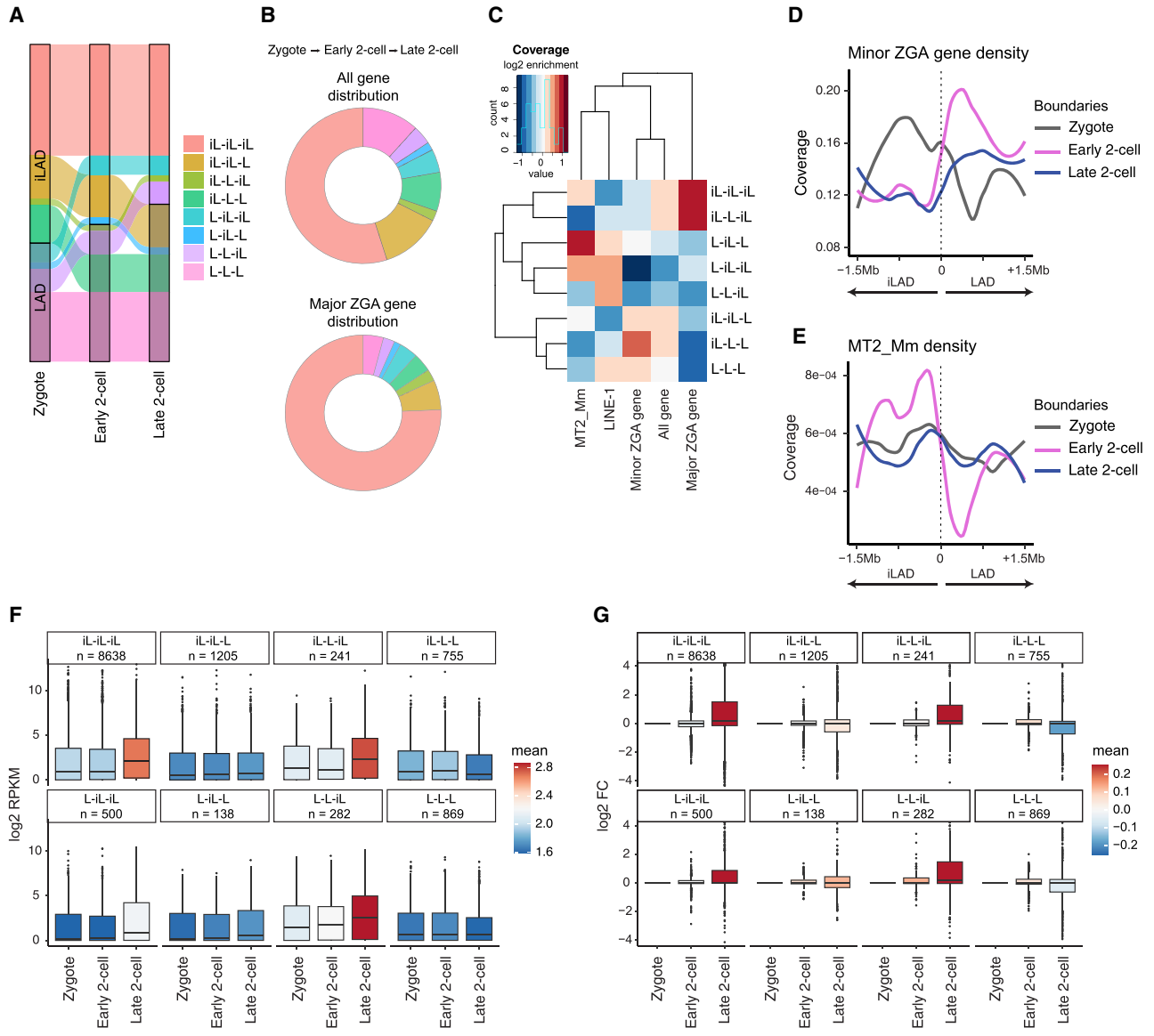

Figure 2. Repositioning of LADs following mitosis correlates with gene and TE class expression. (*A*) Alluvial plot showing LAD reorganization during maternal-to-zygotic transition between zygotes and early and late two-cell stage embryos, respectively. (L) LAD, (iL) inter-LAD. (*B*) Pie charts showing distribution of all genes and major ZGA genes in groups of reorganizing genomic bins. The color code for the groups of reorganizing genomic bins is the same as in *A*. (*C*) Enrichment of genomic features (MT2_Mm, LINE-1, major ZGA, minor ZGA, and all gene coverage) in each group. The average density of all genomic bins was used as expected value. (*D*,*E*) Metaplot of minor ZGA gene density (*D*) and MT2_Mm enrichment (*E*) on LAD boundaries of the corresponding developmental stage. Zero and the dotted line represent the position of the LAD/iLAD boundary in the metaplot, and the 1.5-Mb region at the *right* indicates LAD. (*F*,*G*) Gene expression levels ($\log_2$ RPKM) (*F*) and $\log_2$ fold change of gene expression (*G*) contained within each of the LAD/iLAD pattern groups comparing zygotes with early and late two-cell embryos. Note that we excluded transcripts from maternal genes. Single-cell RNA-seq data were analyzed from GSE45719 (Deng et al. 2014). Box plots show median, and the interquartile range and the plots are colored based on mean values. *n* indicates the number of genes analyzed in each group.

mitosis and along with the progression of the second cell cycle at the two-cell stage.

Because major ZGA starts during the two-cell stage (Jukam et al. 2017; Schulz and Harrison 2019), we next asked whether the genome rearrangements that we observed are associated with the genes activated at ZGA (major ZGA genes) (Park et al. 2015). We found that most major ZGA genes (1111 out of 1462 genes) are located inside constant iLADs (iL-iL-iL; odds ratio 1.4) (Fig. 2B). The remainder of major ZGA genes displayed changes associated with repositioning both from the nuclear interior (iLADs) to the nuclear lamina (LADs) and toward the nuclear interior at the early or late two-cell stage (Fig. 2B). However, ~80% of the major ZGA genes (234 out of

290) that are repositioned in two-cell stage embryos become repositioned to the nuclear interior at either the early or late two-cell stage (Fig. 2B). Thus, while most major ZGA genes are located in iLADs in zygotes and two-cell stage embryos, a proportion of major ZGA genes changes their association with the nuclear lamina at the early and late two-cell stage.

We next performed the opposite analysis and asked whether the genomic regions that become repositioned with respect to the nuclear lamina between the zygote and late two-cell stage embryos are enriched in ZGA genes. Overall, cLADs and iLADs that become LADs in both two-cell stages are depleted of major ZGA genes (L-L-L and iL-L-L) (Fig. 2C) but not minor ZGA genes (Fig. 2C). In addition, the zygotic iLADs that reposition to the nuclear lamina by the end of G1 phase of two-cell stage embryos (iL-L-L) are enriched in minor ZGA genes (odds ratio 1.41) (Fig. 2C). This observation is further supported by the clear switch of minor ZGA gene density from outside the LAD boundary to inside LADs in early two-cell stage embryos (Fig. 2D). Interestingly, we also observed a strong enrichment of MT2_Mm (a MERVL-derived LTR) coverage, but not of LINE-1 elements, in transient early two-cell stage inter-LADs (L-iL-L) (Fig. 2C). Instead, LINE-1 elements are enriched in regions going away from the nuclear lamina from the early to the late two-cell stage (L-iL-iL and L-L-iL) (Fig. 2C), coinciding with their increase in expression levels (Supplemental Fig. S1A; Fadloun et al. 2013; Jachowicz et al. 2017). Notably, MERVL elements shifted their 3D localization completely at this developmental time: Genomic regions just outside the early two-cell stage LAD boundaries became highly enriched in MERVL (MT2_Mm), in contrast to both the zygotic and late two-cell stages, which display neither enrichment nor depletion (Fig. 2E). These data suggest that MERVL elements move toward the nuclear interior (iLADs) at the early two-cell stage, where they are particularly enriched at the LAD–iLAD boundaries. Considering that MERVL elements are highly and transiently expressed at the early two-cell stage (Ishiuchi et al. 2015; Kruse et al. 2019; Liu et al. 2020; Sakashita et al. 2023), these observations establish that the repositioning of MERVL-containing LADs into iLADs at this stage is concordant with their transcriptional activation prior to major ZGA. Thus, we next addressed whether levels of gene expression in general are associated with specific changes of LADs and iLADs that occur during this time window. Because oocytes carry maternal transcripts that accumulate during oocyte growth, we removed maternal genes from our analysis to avoid the confounding effects of oocyte-inherited transcripts present in the zygote. Genes in LADs at the two-cell stage showed the lowest transcript abundance regardless of whether such LADs were cLADs or iLADs prior to the two-cell stage (Fig. 2F). Indeed, changes in gene expression occurred in regions of the genome that repositioned into LADs at the two-cell stage, with a clear reduction in expression from the zygote to the late two-cell stage but notably also when compared with the early two-cell stage (Fig. 2G). Consistent with our observation that most major ZGA genes remain within iLADs (Fig. 2B), we noted a higher expression of associated genes in the late two-cell stage embryos (iL-iL-iL) (Fig 2F,G). Thus, our data indicate a dynamic repositioning of a subset of LADs and iLADs during the two-cell stage that correlates with the transcriptional activity of genes contained therein. In addition, MERVL elements are a unique feature of early two-cell stage iLADs.

Transcriptional inhibition results in large-scale alterations in LADs at the two-cell stage

TAD borders are known to be remodeled to a certain extent by transcriptional activity in cultured cells and in *Drosophila* embryos (Li et al. 2015; Hug et al. 2017; Rowley et al. 2017). However, the extent to which transcriptional activity remodels nuclear architecture in mouse embryos is not fully characterized. Thus, to address directly whether and how transcription during ZGA affects LADs, we performed DamID for LaminB1 in late two-cell stage embryos after incubation with two different RNA polymerase (Pol II) inhibitors: α-amanitin and DRB. While DRB inhibits transcriptional elongation through inhibition of RNA Pol II serine 2 phosphorylation (Dubois et al. 1994), α-amanitin results in full transcriptional inhibition, including via RNA Pol II degradation (Nguyen et al. 1996; Bensaude 2011; T Nakatani, T Schauer, L Altamirano, et al., in prep.). We incubated embryos with either of the two inhibitors continuously from the early zygote stage until the late two-cell stage under conditions known to prevent ZGA (Abe et al. 2018; Liu et al. 2020; T Nakatani, T Schauer, L Altamirano, et al., in prep.) and mapped LADs at this stage (Fig. 3A). PCA revealed that embryos in which ZGA was inhibited clustered together regardless of the inhibitor used and separately from untreated embryos (Fig. 3B). The samples segregated based on their developmental stage along PC2, and both DRB- and α-amanitin-treated late two-cell stage embryos separated from untreated embryos along PC1 and localized closest to the early two-cell stage untreated samples along PC2 (Fig. 3B). These observations suggest that while inhibition of ZGA results in a genome–nuclear lamina interaction profile that is more similar to embryos in which major ZGA has not yet occurred (early two-cell stage), transcriptional inhibition leads also to additional profound alterations (Supplemental Fig. S1B). This suggests that ZGA contributes to the LAD rearrangement that occurs in late two-cell stage embryos but is not the sole determinant of this process. Globally, the genome-wide interactions with the nuclear lamina were affected to a similar extent upon the treatment of the two inhibitors (Spearman's $r = 0.76$) (Fig. 3C), but we noted slightly a stronger effect upon DRB treatment compared with α-amanitin treatment when correlated to both untreated early and late two-cell stage embryos (Fig. 3D,E). This could potentially be due to the differences in the mode of action of the two inhibitors (Bensaude 2011).

Visual inspection of DamID methylation levels and LADs over chromosome tracks revealed that late two-cell stage embryos treated with both α-amanitin and

DRB contain LADs that are less fragmented than the untreated late two-cell stage embryos (Fig. 3F). These data suggest that transcriptional activity underlies the unusual spatial arrangement of LAD patterns in late two-cell stage embryos, characterized by small fragmented LADs (Borsos et al. 2019). To further investigate this, we asked

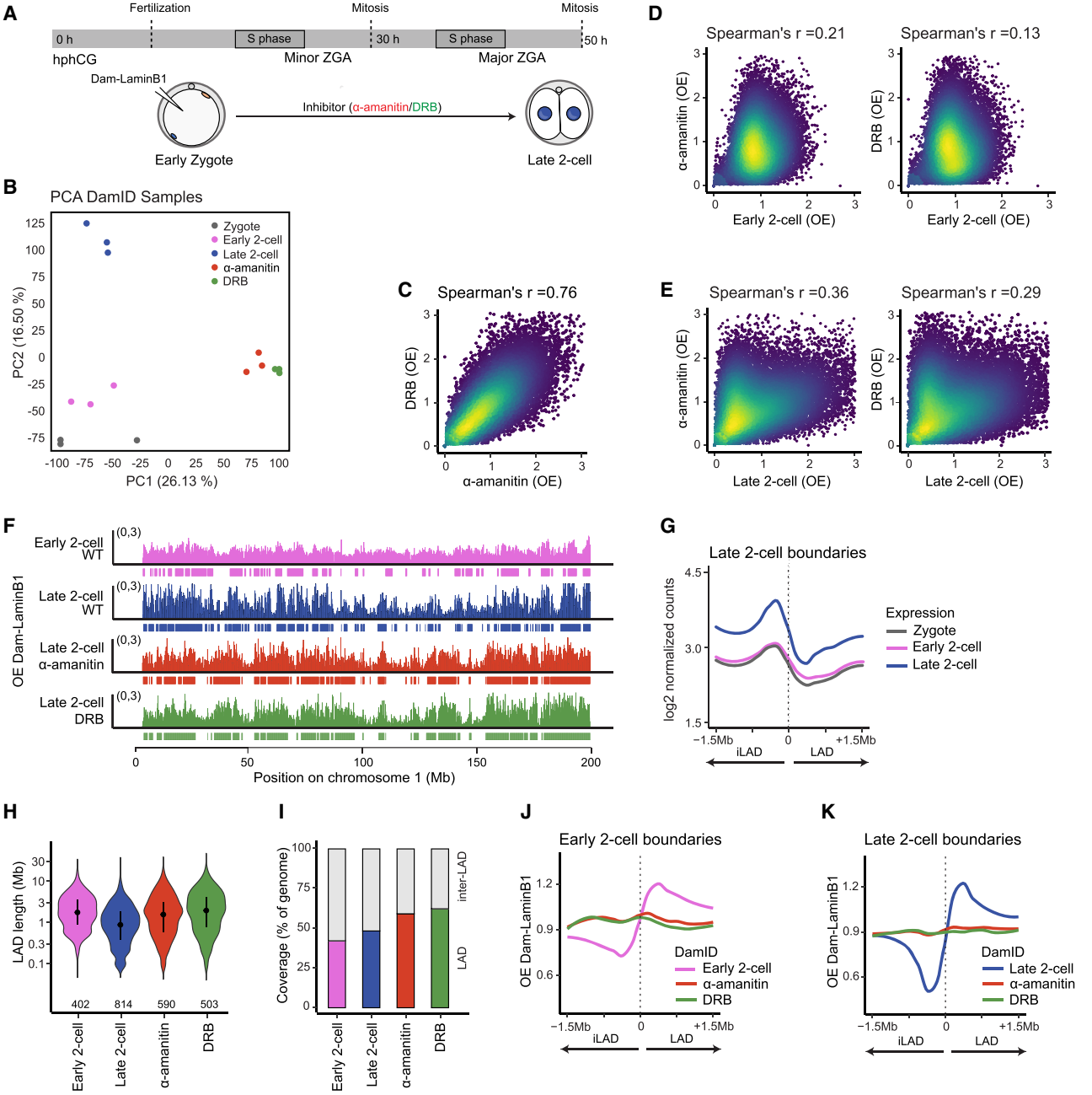

Figure 3. Transcriptional inhibition results in large-scale alterations in two-cell LADs. (*A*) Schematic representation of the experimental design for late two-cell DamID upon inhibition of minor and major waves of ZGA with either α-amanitin or DRB. (hphCG) Hours post-hCG. (*B*) Principal component analysis (PCA) of DamID samples. Each data point represents a biological replicate for the corresponding condition as indicated by the color code. The percentage of variance explained by PC1 and PC2 is indicated in the axis labels. (*C–E*) Genome-wide scatter plot of mean OE values. Spearman's correlation coefficients are indicated. (*F*) Dam-LaminB1 OE mean value profiles and called LADs on chromosome 1 in control (WT) early and late two-cell embryos along with α-amanitin- or DRB-treated late two-cell embryos. (*G*) Average $\log_2$ normalized counts calculated on 100-kb genomic bins for zygotes and early and late two-cell stage embryos analyzed from GSE45719 (Deng et al. 2014) plotted over late two-cell stage LAD boundaries. Zero and the dotted line represent the position of the LAD/iLAD boundary in the metaplot, and the 1.5-Mb region at the *right* indicates LAD. (*H*) Violin plots showing size distribution of LADs. The number of LADs is indicated *below*. (*I*) The percentage of genome coverage of LADs and inter-LADs. (*J,K*) Average Dam-LaminB1 DamID signal over untreated early (*J*) and late (*K*) two-cell stage LAD boundaries.

whether the edges of fragmented LADs are defined by the transcriptional activity, based on RNA-seq, centered over LAD boundaries at the late two-cell stage. Indeed, we found that transcript levels at the late two-cell stage are highest in the proximity of these boundaries compared with the surrounding genomic regions and in comparison with either zygotes or early two-cell stage embryos (Fig. 3G). These analyses suggest that higher transcriptional activity characterizes LAD boundaries at the late two-cell stage. Consistent with a potential role for ZGA in LAD fragmentation, the number of LADs was lower in DRB- and α-amanitin-treated embryos compared with untreated late two-cell stage embryos, while the median LAD length was higher (2 and 1.6 Mb vs. 0.9 Mb, respectively) (Fig. 3H). This resulted in an increased percentage of genome localized into LADs upon DRB and α-amanitin treatment (Fig. 3I). Thus, transcriptional inhibition during ZGA leads to the association of a larger portion of the embryonic genome with the nuclear lamina. Careful examination of LADs on chromosome plots (Fig. 3F) suggested that although the number of LADs after transcriptional inhibition was intermediate between the number of LADs in untreated early and late two-cell stage embryos (Fig. 3H), some changes in the positioning of the LAD boundaries appeared in embryos treated with DRB and α-amanitin. To further investigate this, we plotted the DamID scores of DRB- and α-amanitin-treated two-cell embryos over the early and late two-cell stage boundaries of control embryos. These analyses indicate that treatment with DRB and α-amanitin results in a complete remodeling of wild-type LAD boundaries (Fig. 3J,K).

Atypical features of lamina-associated chromatin emerge upon inhibition of ZGA

To further understand the role of transcription in regulating nuclear organization, we next investigated in more detail the impact of ZGA inhibition on LAD and iLAD rearrangement at the two-cell stage. For this, we first compared LADs and iLADs in α-amanitin-treated embryos with the LADs and iLADs in zygotes and late two-cell stage embryos. While α-amanitin treatment did not affect the repositioning of some genomic regions that typically move toward the nuclear lamina at the two-cell stage (iL-L-L) (Fig. 4A), 36% of zygotic iLADs relocated to the nuclear lamina upon α-amanitin treatment (iL-L-iL) (Fig. 4A). This indicates that α-amanitin treatment precludes the formation of a subset of LADs and iLADs that normally form at the two-cell stage. Interestingly, "de novo LADs" formed in two-cell embryos treated with α-amanitin are enriched in major ZGA genes (iL-L-iL contain 939 out of 1462 major ZGA genes; odds ratio 1.71) (Fig 4B). We obtained similar results with DRB-treated embryos (Supplemental Fig. S1C,D). We found that major ZGA genes are enriched in proximity to zygotic iLAD boundaries (Fig. 4C; Supplemental Fig. S1E), suggesting that regions inside iLADs transform into LADs by transcriptional inhibition. Indeed, we observed that zygotic iLADs, which are enriched for major ZGA genes, become LADs upon α-amanitin or DRB treatment (Fig. 4D; Supplemental Fig. S1E, F). Consequently, major ZGA genes became enriched inside of LAD boundaries in embryos treated with α-amanitin and with DRB, which was not the case in untreated late two-cell stage embryos (Fig. 4C). Thus, we conclude that major ZGA genes relocate to the nuclear lamina upon transcriptional inhibition.

The rearrangement of the genome with respect to the nuclear lamina upon transcriptional inhibition was accompanied by a change in the genomic features of LADs and iLADs. Namely, while LADs are typically characterized by higher AT content compared with iLADs (Meuleman et al. 2013), LADs in α-amanitin- and DRB-treated embryos have lower AT content than iLADs, and this effect is particularly visible close to the LAD boundaries (Fig. 4E). We next investigated the distribution of LINE-1 and SINE B2 elements since they are known to be enriched in LADs and iLADs, respectively, in differentiated cells (Meuleman et al. 2013; Lenain et al. 2017). We found that, in contrast to the controls, LADs become depleted in LINE-1 elements and enriched in SINE B2 elements upon transcriptional inhibition (Fig. 4F; Supplemental Fig. S1G). This was surprising, as it suggested that LINE-1 elements become repositioned toward the nuclear interior in spite of their transcriptional silencing (Supplemental Fig. S1H). We confirmed these observations by performing DNA-FISH for LINE-1, which showed a global visual redistribution of LINE-1 toward the nuclear interior in two-cell stage embryos upon transcriptional inhibition (Supplemental Fig. S1I), validating the DamID data. Thus, the relocalization of LINE-1 elements into iLADs occurs in the absence of transcription.

We also analyzed the levels of H3K4me3, which we previously showed was involved in LAD establishment in zygotes (Borsos et al. 2019). We found that levels of H3K4me3 anticorrelate with LaminB1-DamID methylation levels in control two-cell stage embryos (Fig. 4G), in agreement with our previous observations (Borsos et al. 2019). Because of the known association of H3K4me3 with transcriptional activation (Santos-Rosa et al. 2002), we next asked whether H3K4me3 levels are affected upon inhibition of ZGA and whether those potential alterations relate to the LAD rearrangements that we observed upon transcriptional inhibition. For this, we first reanalyzed publicly available data sets of H3K4me3 from late two-cell stage embryos incubated with α-amanitin (Zhang et al. 2016). Remarkably, visual inspection of H3K4me3 levels across chromosome tracks suggested that α-amanitin treatment led to a redistribution of H3K4me3-marked regions, which highly corresponded to LaminB1-DamID methylation levels (Fig. 4H). Indeed, genome-wide analysis of H3K4me3 enrichment across all LADs and iLADs indicates that while H3K4me3 levels are higher in iLADs in control two-cell stage embryos (Fig. 4I), treatment with α-amanitin and DRB led to a complete reversion of this pattern, with H3K4me3 accumulation at LADs and depletion in iLADs (Fig. 4H,J). These observations suggest that inhibition of ZGA leads to a distribution of the genomic regions that contain H3K4me3 toward the nuclear lamina. We further confirmed this by performing immunostaining for H3K4me3 in late two-cell stage embryos

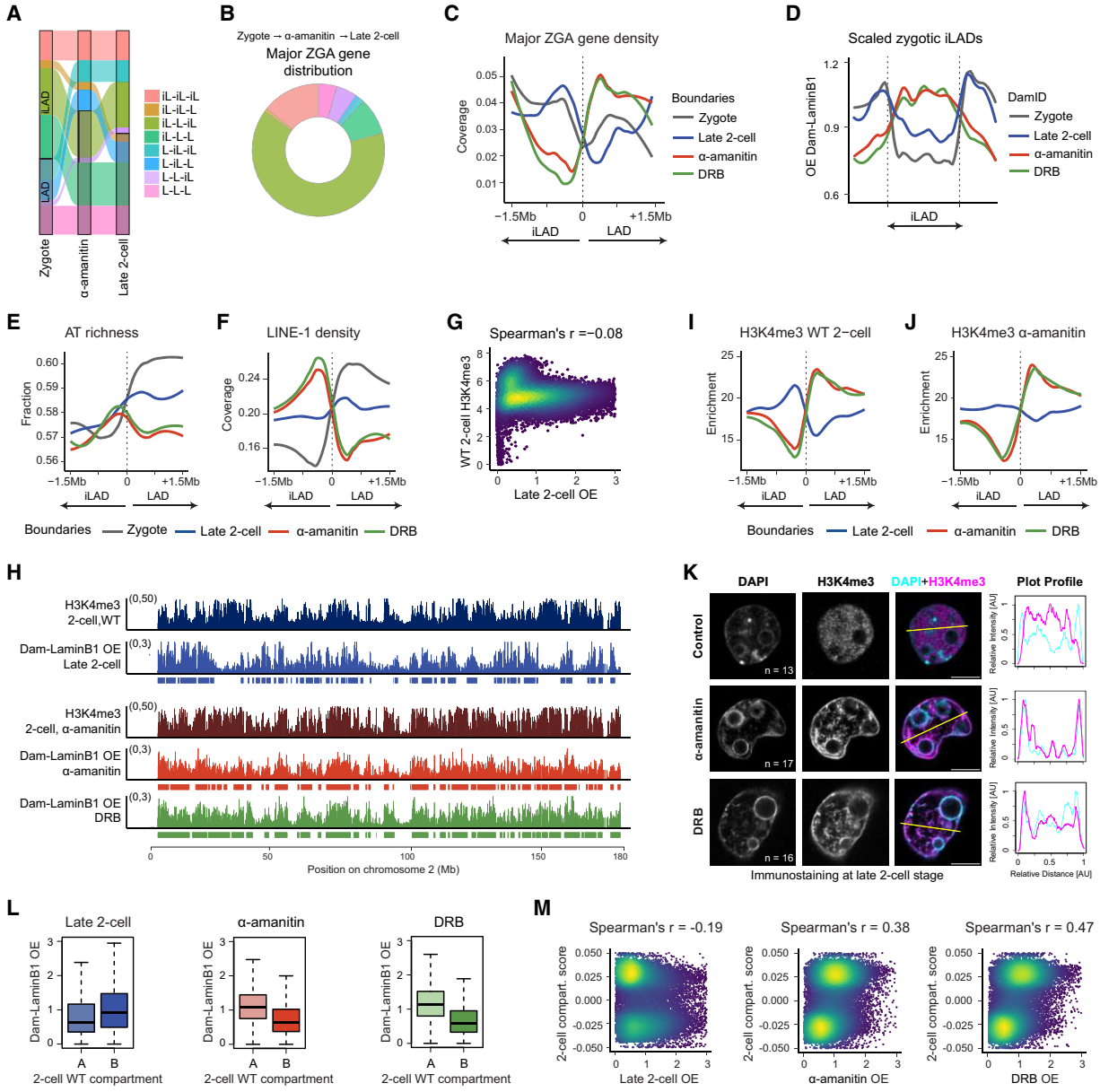

Figure 4. Atypical features of lamina-associated chromatin emerge upon inhibition of ZGA. (*A*,*B*) Alluvial plot and major ZGA gene distribution in reorganizing genomic regions upon transcriptional inhibition with α-amanitin. (*C*) Metaplot of major ZGA gene density over LAD boundaries. Zero and the dotted line represent the position of the LAD/iLAD boundary in the metaplot, and the 1.5-Mb region at the *right* indicates LAD. (*D*) Average LaminB1-DamID signal over scaled zygotic inter-LADs. (*E*,*F*) Average AT content (*E*) and LINE-1 element density (*F*) at LAD boundaries. (*G*) Genome-wide scatter plot of mean DamID OE values and $\log_2$ transformed H3K4me3 enrichment in late two-cell stage embryos. H3K4me3 ChIP-seq data from control (WT) embryos was analyzed from GSE71434 (Zhang et al. 2016). Spearman's correlation coefficient is indicated. (*H*) DamID OE value signal and H3K4me3 enrichment visualized on chromosome 2. H3K4me3 ChIP-seq data sets from control (WT) and α-amanitin-treated late two-cell embryos were analyzed from GSE71434 (Zhang et al. 2016). (*I*,*J*) Metaplots showing average H3K4me3 enrichment on LAD boundaries of untreated late two-cell stage or DRB- and α-amanitin-treated two-cell stage embryos. Please note that in *I*, H3K4me3 data were derived from untreated (WT) late two-cell stage embryos, and in *J*, H3K4me3 data were derived from α-amanitin-treated embryos, but in both panels, the LAD boundary coordinates are from the same samples (late two-cell control [WT] or α-amanitin- or DRB-treated embryos, as indicated by the colored lines). (*K*) Representative single confocal sections from immunostaining of H3K4me3 in control and α-amanitin- and DRB-treated late two-cell embryos (48 h post-hCG). DAPI stains for DNA. *n* = total number of embryos analyzed across three independent experiments. The intensity profiles for the lines shown on the merged images are plotted at the *right*. Scale bars, 10 µm. (*L*) Box plots of Dam-LaminB1 OE values in control (WT) A and B compartment regions. Compartment coordinates were taken from GSE82185 (Du et al. 2017). Box plots show median and the interquartile range (IQR), and whiskers depict the smallest and largest values within 1.5× IQR. (*M*) Genome-wide scatter plot of DamID OE values and compartment score in two-cell stage embryos derived from Hi-C data. The positive compartment (compart.) scores correspond to the A compartment. Spearman's correlation coefficients are indicated.

following DRB and α-amanitin treatment (Fig. 4K). These experiments revealed a drastic change in the localization of H3K4me3: While H3K4me3 is distributed throughout the nucleoplasm in control embryos, it becomes strongly enriched in the nuclear periphery, forming a clear rim around the nucleus in embryos treated with DRB and α-amanitin (Fig. 4K; Supplemental Fig. S2A). We also observed an apparent enrichment of H3K4me3 around the nucleolus precursors (NLBs) after transcriptional inhibition (Fig. 4K; Supplemental Fig. S2A), reflecting the known overlap between LADs and nucleolus-associated domains (NADs) (Bizhanova et al. 2020; Bersaglieri et al. 2022). Analysis of additional histone modifications by immunostaining indicated that other marks typically linked with active transcription, such as H3K9ac, displayed behavior similar to that of H3K4me3 and became visually enriched at the nuclear periphery (Supplemental Fig. S2B). However, a classical repressive histone modification, H3K9me3, did not show this behavior (Supplemental Fig. S2C). Overall, we conclude that inhibition of RNA polymerase II activity in early embryos leads to the rearrangement of H3K4me3-enriched regions and, perhaps more globally, of regions marked by active histone modifications toward the nuclear periphery and the remodeling of LAD boundaries. The mechanism behind this remodeling and whether this may reflect chromatin condensation changes upon global transcriptional inhibition remain to be established. Thus, inhibition of ZGA leads to a change in the genomic and chromatin features of LADs.

Previous work has shown that remodeling of H3K4me3 broad domains to a more canonical pattern after fertilization requires transcriptional activation at ZGA (Zhang et al. 2016). In addition, H3K4me3 broad domains have been postulated to be inhibitory for transcription (Dahl et al. 2016). Thus, we hypothesize that the impaired remodeling of H3K4me3 upon transcriptional inhibition of ZGA results in the sequestration of these domains to the nuclear lamina, in keeping with their transcriptional silent state. While TAD borders are remodeled by transcriptional activity in cultured cells and in *Drosophila* embryos (Li et al. 2015; Rowley et al. 2017), in mouse embryos transcription does not appear to be necessary to consolidate TAD borders and compartments in preimplantation embryos (Du et al. 2017; Ke et al. 2017). However, we found that inhibiting ZGA leads to a drastic remodeling of genome–lamina interactions and of LAD boundaries. To further investigate the relationship between LADs and compartments upon transcriptional inhibition, we analyzed DamID values in A and B compartments in control embryos at the two-cell stage. DamID-LaminB1 values are higher in the B compartments at the two-cell stage in control embryos, as expected (Fig. 4L). However, this pattern is reversed upon α-amanitin and DRB treatment, primarily due to an increase of DamID values within the A compartments but also due to a reduction in lamina interactions of the B compartment regions (Fig. 4L). Indeed, the A compartment regions move toward intermediate Dam-LaminB1 values genome-wide, resulting in a global positive correlation between compartment score and OE values in α-amanitin- and DRB-treated embryos (Fig. 4M). Thus, the A compartment regions gain lamina interactions upon transcriptional inhibition, and overall, compartments display an altered pattern of genome–nuclear lamina interactions upon transcriptional inhibition.

Discussion

Altogether, our data provide novel temporal resolution to the rearrangement of LADs during the maternal-to-zygotic transition and demonstrate that inhibition of transcription during ZGA leads to major changes in LAD organization. Whether a complete transcriptional inhibition in cells in culture also affects LADs has not been investigated and will be interesting to address in the future. It is intriguing that before the major wave of ZGA, in zygotes, LADs show genomic features that are more similar to constitutive LADs across cultured cell types, including LINE-1 enrichment at the nuclear periphery (Fig. 4F; Supplemental Fig. S2D). However, transcriptional inhibition during ZGA leads to unusual features of LADs. LINE-1-enriched genomic regions relocalize toward the nuclear interior, and H3K4me3-marked chromatin starts associating with the nuclear lamina in late two-cell embryos, which is strikingly different from cultured cells or premajor ZGA wild-type zygotes (Supplemental Fig. S2D). This suggests that during maternal-to-zygotic transition, the naturally evolving molecular characteristics of embryonic nuclear organization—in this case of LADs—are dependent on ZGA. From a broader perspective, this implies that the nuclear rearrangement of LADs is an integral component of MZT. The remodeling of nuclear organization after fertilization is considered to be a major event of epigenetic reprogramming occurring at these stages and is not restricted to mice but occurs in other mammals and vertebrates (Pecori and Torres-Padilla 2023). Our results indicate that transcription contributes to the remodeling of one of the pillars of nuclear organization; that is, LAD rearrangement. Interestingly, unlike TADs, LADs are globally unaffected upon inhibition of replication in both zygotes and two-cell stage embryos (Borsos et al. 2019). In contrast, transcriptional inhibition does not affect TAD consolidation (Du et al. 2017; Ke et al. 2017), and thus the contribution of ZGA toward the different pillars of nuclear organization may differ, as well as their dependency toward the different DNA and chromatin-related processes. Future work will determine whether and how other chromatin processes affect nuclear organization.

Our work sheds light onto the molecular mechanisms that occur during fundamental developmental process and how they shape the epigenomic landscape in early mammalian embryogenesis.

Materials and methods

Embryo collection, culture, and manipulation

All experiments were approved by the government of Upper Bavaria. Mice housed in Helmholtz Zentrum München were

maintained and bred in accordance with institutional guidelines. To obtain embryos, 5- to 8-wk-old F1 (C57BL/6J × CBA/H) female mice were mated with DBA/2J males. To induce ovulation, females were injected with 10 IU of pregnant mare serum gonadotropin (PMSG; Ceva) and then 46–48 h later with human chorionic gonadotrophin (hCG; MSD Animal Health). Collected embryos were cultured in KSOM drops under paraffin oil (Sigma) at 37°C with 5% CO_2 as previously described. For DamID in early two-cell embryos, zygotes (18 h post-hCG) were isolated and injected with 250 ng/µL *Tir1*, 50 ng/µL membrane-eGFP, and 10 ng/µL AID-Dam-LaminB1 and cultured in medium containing 500 µM auxin. Auxin was removed just after mitosis for 4–6 h, and early two-cell embryos were collected at 34–36 h post-hCG. For DamID in transcription-inhibited late two-cell embryos, zygotes (18 h post-hCG) were injected with 250 ng/µL *Tir1*, 50 ng/µL membrane-eGFP, and 10 ng/µL AID-Dam-LaminB1-coding mRNA and cultured in KSOM containing 500 µM auxin and either 0.1 mg/mL α-amanitin (BioChemica) or 100 µM DRB (Santa Cruz Biotechnology). To allow methylation of LADs in the late two-cell stage, auxin was washed out from 42 to 48 h post-hCG, and embryos were cultured in KSOM containing either 0.1 mg/mL α-amanitin or 100 µM DRB. For immunofluorescence, zygotes (18 h post-hCG) were isolated and cultured in KSOM containing 0.1 mg/mL α-amanitin or 100 µM DRB until 48 h post-hCG.

DamID sample processing and library preparation

The zona pellucida was removed by treatment with 0.5% pronase in M2 at 37°C. Polar bodies were separated from the embryos by gentle pipetting after trypsin treatment and discarded. For each replicate, a pool of 10–20 blastomeres (five to 10 two-cell embryos) was collected in 2 µL of DamID buffer (10 mM TRIS acetate at pH 7.5, 10 mM magnesium acetate, 50 mM potassium acetate) and stored at −80°C until downstream processing. All experiments were performed in three independent biological replicates. Sample processing and library preparation were done as described previously (Borsos et al. 2019; Pal et al. 2021).

DamID sequencing and analysis

Samples were sequenced using Illumina HiSeq4000 or HiSeq2500 platforms in 150-bp PE mode, but only read1 was used for downstream analysis. For preprocessing of reads, the first six random bases were discarded using trimmomatic (version 0.39). Subsequently, the reads were demultiplexed according to DamID indexes using a Fastx barcode splitter, and the additional 15 bp of adaptors was trimmed using trimmomatic. The preprocessed reads starting with GATC were then mapped to mm10 using bowtie2 (version 2.3.5) with default parameters. Reads aligning to the genome with a quality score <30 were discarded using samtools (version 1.3). Duplicates were removed using picard (version 2.21.1) to finally obtain unique GATC reads. The computation of OE (observed/expected) values per 100-kb bin was carried out as described previously (Kind et al. 2015). LaminB1-DamID data from zygotes and late two-cell stage embryos were obtained from our previous study (GSE112551; Borsos et al. 2019). For data visualization and LAD calling, the OE mean signal of all three replicates was used. To distinguish LADs from inter-LADs, a two-state hidden Markov model (HMM) (Filion et al. 2010) was applied to nonzero OE mean values.

Immunofluorescence

Embryos were fixed in 4% PFA for 20 min at room temperature and permeabilized in PBS containing 0.5% Triton-X for 20 min. Embryos were kept in blocking buffer (3% BSA in PBS) for 4–5 h and then incubated overnight in primary antibody (H3K4me3, 1:250 [Diagenode C15410003]; H3K9ac, 1:250 [Abcam ab4441]; and H3K9me3, 1:100 [Active Motif 39286]) diluted in blocking buffer. After overnight incubation, samples were washed three times in PBS and stained with secondary antibodies conjugated with Alexa fluor 555 or Alexa fluor 647 in blocking buffer for 2–3 h. After three washes in PBS, embryos were mounted in 3D using VectaShield (Vector Laboratories) containing DAPI. Confocal imaging was performed using a 63× oil objective in a Leica SP8 confocal microscope.

Whole-mount DNA-FISH

LINE-1 DNA-FISH was performed as previously described (Jachowicz et al. 2017). LINE-1 probes (L1spa) were labeled with homemade TAMRA-dATP with a nick translation kit (Roche) and purified with a QIAquick PCR purification kit (Qiagen). Confocal imaging was performed using a 63× oil objective in a Leica SP8 confocal microscope.

Image analysis

Image analysis was performed with ImageJ software's plot profile function. Example lines for obtaining intensity profiles were drawn manually, avoiding NLBs. The results were then processed and plotted using R (version 4.1.2). Intensity values were smoothed using the rollmean function with $k = 21$ from the zoo package (version 1.8–12). Smoothed values were minimum/maximum-scaled such that the final values ranged between 0 and 1.

RNA-seq analysis

The RNA-seq data set for wild-type zygotes and early and late two-cell stage embryos was obtained from GEO with accession number GSE45719 (Deng et al. 2014), processed expression values (RPKM) were downloaded, and the mean RPKM for each developmental stage was calculated. DBTMEE maternal RNA genes (Park et al. 2015) were excluded from RPKM and $\log_2$ fold change analysis of RNA-seq data. For metaplot analysis of RNA-seq data, reads were aligned to the GRCm38 reference genome using STAR (version 2.7.6a), and mapped reads were counted in 100-kb genomic bins using the GenomicAlignments (version 1.30.0) and GenomicRanges (version 1.46.1) R packages. Read counts were normalized to the total number of reads and multiplied by 1 million. Metaplots at LAD boundaries were generated on the $\log_2$ normalized counts using custom R scripts. RNA-seq data for α-amanitin and control two-cell stage embryos were obtained from GEO with accession number GSE72784 (Dahl et al. 2016).

Analysis of transposable elements and ZGA genes

TE annotation for the mm10 genome was obtained from the Hammell laboratory repository (https://labshare.cshl.edu/shares/mhammelllab/www-data/TEtranscripts/TE_GTF/mm10_rmsk_TE.gtf.gz). A list of minor and major ZGA genes was considered according to DBTMEE (Park et al. 2015) classification. TE and ZGA gene density was calculated using the bedtools (version 2.31.0) coverage function in 100-kb genomic bins (same resolution as DamID). Metaplots on LAD boundaries were generated using deepTools. For enrichment analysis of TEs and ZGA genes in reorganizing genomic bins, the average density of all genomic bins was used as the expected value. TE expression analysis from RNA-seq data was performed using TEtranscripts (version 2.2.3, https://github.com/mhammell-laboratory/TEtranscripts). Briefly, reads were aligned

to the GRCm38 reference genome using STAR (version 2.7.6a) with parameters --outFilterMultimapNmax 100 and --winAnchorMultimapNmax 100. Reads were counted at genes and TEs using TEcount with parameters --mode multi and --stranded no. Read counts were normalized by a normalization factor that was the total sum of the reads per sample divided by the mean total sum of all samples. After $\log_2$ transformation, the median of all LINE-1 family elements was taken for each sample and visualized as a dot plot.

Hi-C data analysis

Hi-C compartment coordinates and scores were obtained from GEO with accession number GSE82185 (Du et al. 2017) and analyzed as described in Borsos et al. (2019).

Analysis of H3K4me3 data sets

H3K4me3 ChIP-seq data sets were downloaded from GEO with accession number GSE71434 (Zhang et al. 2016). After trimming, reads were aligned to the GRCm38 reference genome using bowtie2 (version 2.3.5). Reads were filtered by mapping quality score using samtools (version 1.3) with parameter -q 12. Read pairs were read into R using the readGAlignmentPairs function from the GenomicAlignment package (version 1.30.0) and were filtered for unique fragments. Fragments were counted in 50-kb consecutive genomic bins, normalized by the sum of the fragments counts, and multiplied by 1 million. Metaplots on LAD boundaries were generated using deepTools.

Data availability

DamID data sets generated in this study have been deposited in GEO under accession number GSE241483.

Competing interest statement

The authors declare no competing interests.

Acknowledgments

We thank T. Nakatani and A. Burton for critical reading of the manuscript, and I. de la Rosa Velazquez at the Helmholtz Munich Genomics Facility and H. Holcini and C. Lefebvre at the Laboratoire de Génomique of the Hôpital Henri Modor for sequencing. Work in the Torres-Padilla laboratory is funded through the Helmholtz Association, the German Research Foundation (DFG) Project-ID 213249687 (SFB 1064), and the National Institutes of Health 4DN program (grant no. 5U01DK127391-03). M.P. was partially supported by the Marie Curie actions program "ChromDesign" (grant no. 813327).

Author contributions: M.P. performed all experimental work and designed the study. M.P., L.A.-P., and T.S. performed computational analyses. M.-E.T.-P. designed, conceived, and supervised the study.

References

Abe K, Funaya S, Tsukioka D, Kawamura M, Suzuki Y, Suzuki MG, Schultz RM, Aoki F. 2018. Minor zygotic gene activation is essential for mouse preimplantation development. *Proc Natl Acad Sci* **115:** E6780–E6788. doi:10.1073/pnas.1805239115

Bensaude O. 2011. Inhibiting eukaryotic transcription. which compound to choose? How to evaluate its activity? *Transcription* **2:** 103–108. doi:10.4161/trns.2.3.16172

Bersaglieri C, Kresoja-Rakic J, Gupta S, Bär D, Kuzyakiv R, Panatta M, Santoro R. 2022. Genome-wide maps of nucleolus interactions reveal distinct layers of repressive chromatin domains. *Nat Commun* **13:** 1483. doi:10.1038/s41467-022-29146-2

Bizhanova A, Yan A, Yu J, Zhu LJ, Kaufman PD. 2020. Distinct features of nucleolus-associated domains in mouse embryonic stem cells. *Chromosoma* **129:** 121–139. doi:10.1007/s00412-020-00734-9

Borsos M, Perricone SM, Schauer T, Pontabry J, de Luca KL, de Vries SS, Ruiz-Morales ER, Torres-Padilla M-E, Kind J. 2019. Genome–lamina interactions are established de novo in the early mouse embryo. *Nature* **569:** 729–733. doi:10.1038/s41586-019-1233-0

Burton A, Torres-Padilla M-E. 2014. Chromatin dynamics in the regulation of cell fate allocation during early embryogenesis. *Nat Rev Mol Cell Biol* **15:** 723–735. doi:10.1038/nrm3885

Burton A, Brochard V, Galan C, Ruiz-Morales ER, Rovira Q, Rodriguez-Terrones D, Kruse K, Le Gras S, Udayakumar VS, Chin HG, et al. 2020. Heterochromatin establishment during early mammalian development is regulated by pericentromeric RNA and characterized by non-repressive H3K9me3. *Nat Cell Biol* **22:** 767–778. doi:10.1038/s41556-020-0536-6

Dahl JA, Jung I, Aanes H, Greggains GD, Manaf A, Lerdrup M, Li G, Kuan S, Li B, Lee AY, et al. 2016. Broad histone H3K4me3 domains in mouse oocytes modulate maternal-to-zygotic transition. *Nature* **537:** 548–552. doi:10.1038/nature19360

Deng Q, Ramsköld D, Reinius B, Sandberg R. 2014. Single-cell RNA-seq reveals dynamic, random monoallelic gene expression in mammalian cells. *Science* **343:** 193–196. doi:10.1126/science.1245316

Du Z, Zheng H, Huang B, Ma R, Wu J, Zhang X, He J, Xiang Y, Wang Q, Li Y, et al. 2017. Allelic reprogramming of 3D chromatin architecture during early mammalian development. *Nature* **547:** 232–235. doi:10.1038/nature23263

Dubois M-F, Bellier S, Seo S-J, Bensaude O. 1994. Phosphorylation of the RNA polymerase II largest subunit during heat shock and inhibition of transcription in HeLa cells. *J Cell Physiol* **158:** 417–426. doi:10.1002/jcp.1041580305

Fadloun A, Le Gras S, Jost B, Ziegler-Birling C, Takahashi H, Gorab E, Carninci P, Torres-Padilla M-E. 2013. Chromatin signatures and retrotransposon profiling in mouse embryos reveal regulation of LINE-1 by RNA. *Nat Struct Mol Biol* **20:** 332–338. doi:10.1038/nsmb.2495

Filion GJ, van Bemmel JG, Braunschweig U, Talhout W, Kind J, Ward LD, Brugman W, de Castro IJ, Kerkhoven RM, Bussemaker HJ, et al. 2010. Systematic protein location mapping reveals five principal chromatin types in *Drosophila* cells. *Cell* **143:** 212–224. doi:10.1016/j.cell.2010.09.009

Flyamer IM, Gassler J, Imakaev M, Brandão HB, Ulianov SV, Abdennur N, Razin SV, Mirny LA, Tachibana-Konwalski K. 2017. Single-nucleus Hi-C reveals unique chromatin reorganization at oocyte-to-zygote transition. *Nature* **544:** 110–114. doi:10.1038/nature21711

Hug CB, Grimaldi AG, Kruse K, Vaquerizas JM. 2017. Chromatin architecture emerges during zygotic genome activation independent of transcription. *Cell* **169:** 216–228.e19. doi:10.1016/j.cell.2017.03.024

Ishiuchi T, Enriquez-Gasca R, Mizutani E, Bošković A, Ziegler-Birling C, Rodriguez-Terrones D, Wakayama T, Vaquerizas JM, Torres-Padilla M-E. 2015. Early embryonic-like cells are induced by downregulating replication-dependent chromatin

assembly. *Nat Struct Mol Biol* **22:** 662–671. doi:10.1038/nsmb.3066

Jachowicz JW, Bing X, Pontabry J, Bošković A, Rando OJ, Torres-Padilla M-E. 2017. LINE-1 activation after fertilization regulates global chromatin accessibility in the early mouse embryo. *Nat Genet* **49:** 1502–1510. doi:10.1038/ng.3945

Jukam D, Shariati SAM, Skotheim JM. 2017. Zygotic genome activation in vertebrates. *Dev Cell* **42:** 316–332. doi:10.1016/j.devcel.2017.07.026

Ke Y, Xu Y, Chen X, Feng S, Liu Z, Sun Y, Yao X, Li F, Zhu W, Gao L, et al. 2017. 3D chromatin structures of mature gametes and structural reprogramming during mammalian embryogenesis. *Cell* **170:** 367–381.e20. doi:10.1016/j.cell.2017.06.029

Kind J, Pagie L, Ortabozkoyun H, Boyle S, de Vries SS, Janssen H, Amendola M, Nolen LD, Bickmore WA, van Steensel B. 2013. Single-cell dynamics of genome-nuclear lamina interactions. *Cell* **153:** 178–192. doi:10.1016/j.cell.2013.02.028

Kind J, Pagie L, de Vries SS, Nahidiazar L, Dey SS, Bienko M, Zhan Y, Lajoie B, de Graaf CA, Amendola M, et al. 2015. Genome-wide maps of nuclear lamina interactions in single human cells. *Cell* **163:** 134–147. doi:10.1016/j.cell.2015.08.040

Kruse K, Díaz N, Enriquez-Gasca R, Gaume X, Torres-Padilla M-E, Vaquerizas JM. 2019. Transposable elements drive reorganisation of 3D chromatin during early embryogenesis. bioRxiv doi:10.1101/523712

Lenain C, de Graaf CA, Pagie L, Visser NL, de Haas M, de Vries SS, Peric-Hupkes D, van Steensel B, Peeper DS. 2017. Massive reshaping of genome-nuclear lamina interactions during oncogene-induced senescence. *Genome Res* **27:** 1634–1644. doi:10.1101/gr.225763.117

Li L, Lu X, Dean J. 2013. The maternal to zygotic transition in mammals. *Mol Aspects Med* **34:** 919–938. doi:10.1016/j.mam.2013.01.003

Li L, Lyu X, Hou C, Takenaka N, Nguyen HQ, Ong C-T, Cubeñas-Potts C, Hu M, Lei EP, Bosco G, et al. 2015. Widespread rearrangement of 3D chromatin organization underlies Polycomb-mediated stress-induced silencing. *Mol Cell* **58:** 216–231. doi:10.1016/j.molcel.2015.02.023

Liu X, Wang C, Liu W, Li J, Li C, Kou X, Chen J, Zhao Y, Gao H, Wang H, et al. 2016. Distinct features of H3K4me3 and H3K27me3 chromatin domains in pre-implantation embryos. *Nature* **537:** 558–562. doi:10.1038/nature19362

Liu B, Xu Q, Wang Q, Feng S, Lai F, Wang P, Zheng F, Xiang Y, Wu J, Nie J, et al. 2020. The landscape of RNA Pol II binding reveals a stepwise transition during ZGA. *Nature* **587:** 139–144. doi:10.1038/s41586-020-2847-y

Meuleman W, Peric-Hupkes D, Kind J, Beaudry J-B, Pagie L, Kellis M, Reinders M, Wessels L, van Steensel B. 2013. Constitutive nuclear lamina–genome interactions are highly conserved and associated with A/T-rich sequence. *Genome Res* **23:** 270–280. doi:10.1101/gr.141028.112

Nguyen VT, Giannoni F, Dubois M-F, Seo S-J, Vigneron M, Kédinger C, Bensaude O. 1996. In vivo degradation of RNA polymerase II largest subunit triggered by α-amanitin. *Nucleic Acids Res* **24:** 2924–2929. doi:10.1093/nar/24.15.2924

Pal M, Kind J, Torres-Padilla M-E. 2021. DamID to map genome–protein interactions in preimplantation mouse embryos *Methods Mol Biol* **2214:** 265–282. doi:10.1007/978-1-0716-0958-3_18

Park S-J, Shirahige K, Ohsugi M, Nakai K. 2015. DBTMEE: a database of transcriptome in mouse early embryos. *Nucleic Acids Res* **43:** D771–D776. doi:10.1093/nar/gku1001

Peaston AE, Evsikov AV, Graber JH, de Vries WN, Holbrook AE, Solter D, Knowles BB. 2004. Retrotransposons regulate host genes in mouse oocytes and preimplantation embryos. *Dev Cell* **7:** 597–606. doi:10.1016/j.devcel.2004.09.004

Pecori F, Torres-Padilla M-E. 2023. Dynamics of nuclear architecture during early embryonic development and lessons from liveimaging. *Dev Cell* **58:** 435–449. doi:10.1016/j.devcel.2023.02.018

Peric-Hupkes D, Meuleman W, Pagie L, Bruggeman SWM, Solovei I, Brugman W, Gräf S, Flicek P, Kerkhoven RM, van Lohuizen M, et al. 2010. Molecular maps of the reorganization of genome–nuclear lamina interactions during differentiation. *Mol Cell* **38:** 603–613. doi:10.1016/j.molcel.2010.03.016

Rowley MJ, Nichols MH, Lyu X, Ando-Kuri M, Rivera ISM, Hermetz K, Wang P, Ruan Y, Corces VG. 2017. Evolutionarily conserved principles predict 3D chromatin organization. *Mol Cell* **67:** 837–852.e7. doi:10.1016/j.molcel.2017.07.022

Sakashita A, Kitano T, Ishizu H, Guo Y, Masuda H, Ariura M, Murano K, Siomi H. 2023. Transcription of MERVL retrotransposons is required for preimplantation embryo development. *Nat Genet* **55:** 484–495. doi:10.1038/s41588-023-01324-y

Santos-Rosa H, Schneider R, Bannister AJ, Sherriff J, Bernstein BE, Emre NCT, Schreiber SL, Mellor J, Kouzarides T. 2002. Active genes are tri-methylated at K4 of histone H3. *Nature* **419:** 407–411. doi:10.1038/nature01080

Schultz RM. 2002. The molecular foundations of the maternal to zygotic transition in the preimplantation embryo. *Hum Reprod Update* **8:** 323–331. doi:10.1093/humupd/8.4.323

Schulz KN, Harrison MM. 2019. Mechanisms regulating zygotic genome activation. *Nat Rev Genet* **20:** 221–234. doi:10.1038/s41576-018-0087-x

van Schaik T, Vos M, Peric-Hupkes D, Celie PHN, van Steensel B. 2020. Cell cycle dynamics of lamina-associated DNA. *EMBO Rep* **21:** e50636. doi:10.15252/embr.202050636

van Steensel B, Belmont AS. 2017. Lamina-associated domains: links with chromosome architecture, heterochromatin and gene repression. *Cell* **169:** 780–791. doi:10.1016/j.cell.2017.04.022

Vastenhouw NL, Cao WX, Lipshitz HD. 2019. The maternal-to-zygotic transition revisited. *Development* **146:** dev161471. doi:10.1242/dev.161471

Wang C, Liu X, Gao Y, Yang L, Li C, Liu W, Chen C, Kou X, Zhao Y, Chen J, et al. 2018. Reprogramming of H3K9me3-dependent heterochromatin during mammalian embryo development. *Nat Cell Biol* **20:** 620–631. doi:10.1038/s41556-018-0093-4

Xia W, Xie W. 2020. Rebooting the epigenomes during mammalian early embryogenesis. *Stem Cell Rep* **15:** 1158–1175. doi:10.1016/j.stemcr.2020.09.005

Zeng F, Schultz RM. 2005. RNA transcript profiling during zygotic gene activation in the preimplantation mouse embryo. *Dev Biol* **283:** 40–57. doi:10.1016/j.ydbio.2005.03.038

Zhang B, Zheng H, Huang B, Li W, Xiang Y, Peng X, Ming J, Wu X, Zhang Y, Xu Q, et al. 2016. Allelic reprogramming of the histone modification H3K4me3 in early mammalian development. *Nature* **537:** 553–557. doi:10.1038/nature19361